Research Square

Preprints are preliminary reports that have not undergone peer review.
They should not be considered conclusive, used to inform clinical practice,
or referenced by the media as validated information.

Natural van der Waals silicates as hosts for telecom quan- tum emitters: the case of erbium-doped talc

Gellért Dolecsek
Eötvös Loránd University
Zsolt Benedek
Eötvös Loránd University
Nguyen Tien Son
Linköping University
Viktor Ivády
ivady.viktor@ttk.elte.hu

Eötvös Loránd University

Article

Keywords:

Posted Date: September 23rd, 2026

DOI: https://doi.org/10.21203/rs.3.rs-10915079/v1

License: This work is licensed under a Creative Commons Attribution 4.0 International License.
Read Full License

Additional Declarations: No competing interests reported.

Natural van der Waals silicates as hosts for telecom quantum emitters: the case of erbium-doped talc

Gellért Dolecsek[1,2], Zsolt Benedek[1,2], Nguyen Tien Son[3], Viktor Ivády[1,2,*]

[1]*Department of Physics of Complex Systems, Eötvös Loránd University, Egyetem tér 1-3, H-1053 Budapest, Hungary*

[2]*MTA–ELTE Lendület "Momentum" NewQubit Research Group, Pázmány Péter, Sétány 1/A, 1117 Budapest, Hungary*

[3]*Department of Physics, Chemistry and Biology, Linköping University, 58183 Linköping, Sweden*

**email: ivady.viktor@ttk.elte.hu*

August 11, 2026

Erbium ion is among the most promising solid-state single photon emitters and spin-photon interfaces for quantum networks, emitting directly in the telecom C-band in many host semiconductors. Recently, the search for scalable, low-noise host materials turned toward atomically thin and van der Waals materials that enable efficient integration with nanophotonic architectures. Here, we identify talc, a naturally occurring layered magnesium silicate, as a promising host for telecom-active erbium centers. Using first-principles density functional theory combined with multireference wavefunction calculations, we investigate the thermodynamic stability, electronic structure, crystal-field splitting, and optical transitions of erbium-related defects in talc. We find that substitutional incorporation of Er at Mg sites is energetically favourable over a wide range of Fermi-levels, leading predominantly to telecom C band emitting Er^{3+} configuration. The characteristic $^4I_{13/2} \rightarrow {}^4I_{15/2}$ transition of Er^{3+} is preserved in the talc environment and remains centred near 1.55 μm, while crystal-field interactions produce a Stark manifold suitable for spectrally selective optical addressing. The combination of thermodynamic stability, wide band gap, low background emission, and compatibility with van der Waals heterostructures suggests that erbium-doped talc constitutes a

promising platform for integrated photonics in the C-band.

Introduction

Rare earth elements (REEs), which consist of scandium, yttrium, and the 15 lanthanides[1], are most commonly present in the environment in the form of REE^{3+} ions[2,3]. In these chemical structures, the 4f electronic subshell is partially filled, and its electrons are strongly shielded by the outer 5s and 5p subshells[2,3]. Therefore, 4f electrons hardly participate in chemical bonding and are only weakly affected by the surrounding environment[2].

The intra-4f transitions of rare-earth ions are widely exploited in photonic and optoelectronic technologies[2,3]. In particular, rare-earth-doped materials serve as active media in solid-state lasers, optical amplifiers, and infrared-to-visible upconversion for lighting and displays[3–5]. Their long-lived and spectrally sharp luminescence is also used in optical sensing, time-resolved bioimaging, and security marking devices[3,6,7].

In recent years, potential quantum applications have also been demonstrated. Single-photon emission from individual rare-earth ions has been experimentally observed[8–12] and has already been used to demonstrate single-ion spin-photon entanglement[13]. For the time being, active research is conducted targeting rare-earth-ion quantum repeaters, scalable networks, and practical rare-earth single-photon sources[10,14–16].

Among the 4f-related optical transitions of REEs, the photoemission of the erbium cation (Er^{3+}) deserves particular interest: the characteristic zero-phonon line (ZPL) of Er^{3+} appears near 1550 nm in many hosts[5,11,17–21] lying within the telecommunication wavelength range of 1260-1675 nm (0.74-0.98 eV). Moreover, indistinguishable single photon emission[11,21], optically detected magnetism resonance (ODMR), spin-photon interface, single-shot readout, and 23 ms long coherence time of Er^{3+} spin qubits have been demonstrated[22–24]. Furthermore, erbium-doped optical fibers were suggested to be applicable as quantum memory and light storage platforms [25].

Recently, two-dimensional and van der Waals materials have attracted considerable interest because their atomically thin geometry enables unusual electronic, optical, spin, and valley properties, as well as assembly into layered heterostructures[26–30]. Their accessible surfaces and efficient coupling to nearby photonic structures also make them promising hosts for optically active de-

fects and quantum emitters[31,32]. In the case of Er^{3+} ions as dopants, the incorporation into a 2D host has already been demonstrated in WS_2, producing telecom-range emission and illustrating the potential of rare-earth-doped van der Waals materials[19].

Graphene and hexagonal boron nitride are currently among the most prominent deliberately prepared or mechanically exfoliated 2D materials in materials and quantum science[26,33,34]. However, layered van der Waals structures also occur naturally in abundant silicates, including muscovite, biotite, phlogopite, lepidolite, and talc, which can be exfoliated into thin flakes[35,36]. These minerals therefore, provide a complementary route toward chemically stable 2D platforms without requiring epitaxial or bottom-up synthesis.

Motivated by a previous theoretical study of our group [36], we herein suggest talc as a promising alternative host for Er^{3+} centers. Talc is a wide-band-gap magnesium silicate with a low concentration of optically active intrinsic defects, which may suppress host absorption, optical background, and charge fluctuation, potentially enabling lifetime-limited line widths for emitters.[36]. Its atomically flat, dangling-bond-free surfaces and exfoliability[35] facilitate the integration and controlled positioning of optically active centers in van der Waals heterostructures and hybrid photonic devices[37–39]. In particular, an Er-doped talc flake could be placed near the optical-field maximum of an external dielectric or photonic-crystal cavity, making it suitable for Purcell-enhanced emission despite the moderate refractive index of talc itself[32,40]. Furthermore, being the softest crystal (1 on the Mohs Hardness Scale), talc facilitates the creation of high-quality factor cavities and potentially enables talc-based quantum optics.

Despite their apparent potential, very little is known about the REEs in talc. In the present study, we apply density functional theory (DFT) and wavefunction theory (WFT) calculations to characterize erbium structures embedded in talc. After assessing the conceivable configurations and charge states of Er in talc, we investigate their formation energy, electronic structure, optical properties, and the effect of the talc environment on the telecom-band photoemission. Our results demonstrate the practical applicability of hosting Er^{3+} in talc, which opens the path for developing novel quantum optics and nano photonic applications in talc quasi-2D layers.

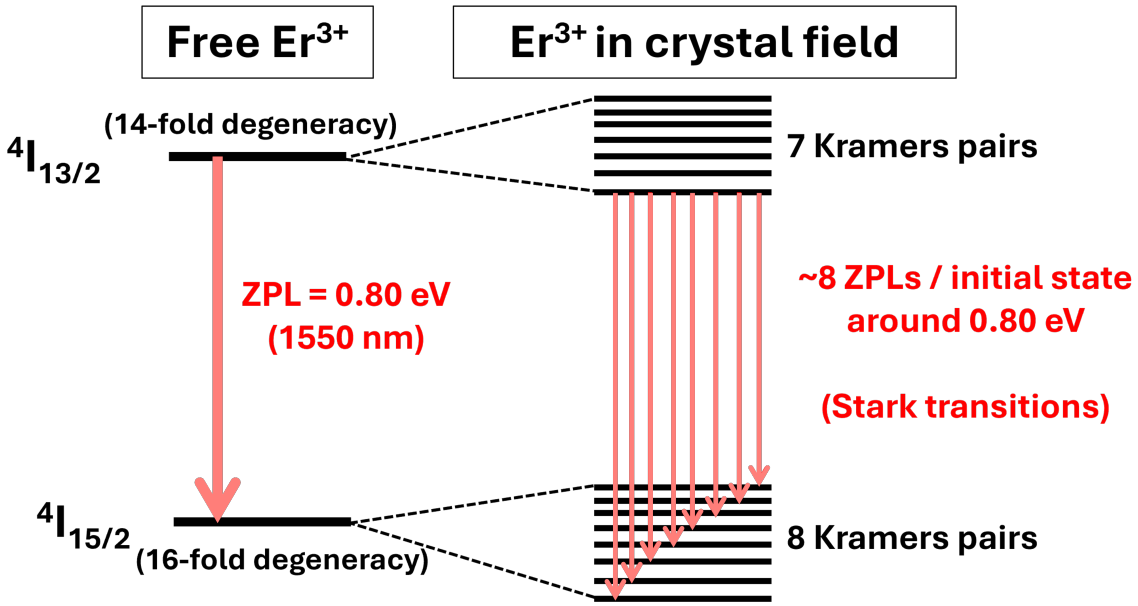

Figure 1: Schematic representation of the lowest-lying spin-orbit coupled energy levels of the free Er^{3+} ion (left) and a crystal-embedded Er^{3+} ion (right).

Background. The well-characterized 1550 nm emission of the Er^{3+} ion is not related to any HOMO–LUMO-type excitation. Instead, the optical transition occurs within the $4f^{11}$ configuration, between two spin orbit-coupled manifolds[17,41,42]. The free Er^{3+} ion has 11 electrons (in other words, 3 holes) distributed over the 7 orbitals of the 4f subshell. According to Hund's first, second and third rules, the ground state is ${}^4I_{15/2}$ with a quartet spin $((2S+1)=4)$ due to three unpaired electrons, with total orbital angular momentum $L=6$ (corresponding to the I term, which can be viewed, in the hole picture, as arising from the maximally allowed individual m_l quantum numbers of 3, 2 and 1) and total angular momentum $J=15/2$, which is the highest possible quantum number within the $(L-S),\ldots,(L+S)$ range for the more-than-half-filled $4f^{11}$ shell. The lowest-lying excited manifold, ${}^4I_{13/2}$, possesses the same S and L quantum numbers, but a decreased J of 13/2. Therefore, the origin of the telecom band emission is the ${}^4I_{13/2} \rightarrow {}^4I_{15/2}$ relaxation[17,41,43]. For such a transition, the photoluminescence spectrum is expected to contain a single sharp ZPL, with negligible phonon sideband due to the absence of geometry relaxation effects.

In free Er^{3+} ions, the aforementioned $(2J+1)$-fold degeneracy is exact, apart from hyperfine interactions and external fields (Fig. 1, left). In a crystal field, however, states belonging to the same J manifold lose their degeneracy. Since Er^{3+} is a Kramers ion with an odd number of 4f electrons, each Stark level remains at least doubly degenerate, and a low-symmetry crystal field can split a half-integer-J manifold into up to $(J + 1/2)$ Kramers pairs (Fig. 1, right)[41,42]. Consequently, multiple zero-phonon lines are expected in the photoluminescence spectrum, corresponding to transitions between Stark components of the $^4I_{13/2}$ and $^4I_{15/2}$ manifolds[17,43]. The actual number of observed lines also depends on site symmetry and experimental conditions, such as spectral resolution and temperature[43]. Such splitting does not prevent conventional optoelectronic use of Er^{3+} emission; in fact, it contributes to the spectral structure and bandwidth of Er-doped optical amplifiers. Quantum applications, however, require a well-defined narrow emission line, i.e., one selected Stark transition. To date, reported Er^{3+}-based single-ion single-photon sources have relied on Purcell enhancement of selected optical transitions[8,10–12].

Er^{3+} has been incorporated into diverse solid-state hosts, most prominently silica glasses and optical fibers, which offer chemical and thermal stability, telecom transparency, low optical loss, and mature processing technologies[5,17]. Common crystalline hosts include Y_2SiO_5, Y_2O_3, YVO_4, $CaWO_4$, and $LiNbO_3$, selected for their ordered and stable rare-earth coordination environments, low disorder, and good optical transparency[11,44–47]. $LiNbO_3$ additionally provides strong electro-optic response and established waveguide-fabrication routes[48,49]. Er^{3+} has also been incorporated into TiO_2, CeO_2, and other epitaxial or thin-film oxides suitable for thin-film growth and nanophotonic integration[46,50,51]. Less conventional semiconductor hosts, including silicon and SiC, provide compatibility with semiconductor processing, although their Er centers are strongly influenced by local defects, charge compensation, and coordination[52–56].

Quantum-optical applications have been pursued prominently in Er^{3+}:Y_2SiO_5 for ensemble quantum memories[15,57], in Er^{3+}:$CaWO_4$ for single-ion spin-photon interfaces and indistinguishable-photon generation[11,13], and in $LiNbO_3$ and silicon for integrated single-ion and cavity-coupled photonics[8,10,49,52–54]. Emerging quantum-oriented studies have also considered epitaxial oxide hosts and SiC[46,50,51,56].

In all these hosts, the relevant telecom photoluminescence is assigned to the shielded intra-4f $^4I_{13/2} \rightarrow {}^4I_{15/2}$ transition of Er^{3+} near 1.5-1.6 μm, however, the exact wavelength, Stark structure, linewidth, and lifetime are host-dependent[17,41,45]. Representative bulk or weakly coupled excited-state lifetimes, referring to the total decay of the $^4I_{13/2}$ manifold through all allowed Stark-resolved emission channels rather than to a single zero-phonon line, are approximately 10 ms in silica fibers[17], 11.4 and 9.2 ms for the two Er^{3+} sites in Y_2SiO_5[45], and a few to several milliseconds in $CaWO_4$, with reported values depending on site, sample preparation, temperature, and concentration[58,59]. In $LiNbO_3$, uncoupled Er^{3+} centers generally exhibit millisecond-scale total excited-state lifetimes, typically of order 2-6 ms depending on the material and processing route[49,60,61]. For quantum applications, however, the relevant quantity is often the radiative rate and branching ratio of one selected Stark-to-Stark ZPL. Optical cavities can selectively enhance such a transition through the Purcell effect and thereby reduce the measured total lifetime to tens of microseconds or, in strongly enhanced structures, a few microseconds; values around 10 μs have been reported for cavity-coupled $LiNbO_3$[10], with a comparable microsecond-to-tens-of-microseconds range demonstrated in $CaWO_4$ nanophotonic devices[11,13].

Results

Erbium related defects in talc. One layer of talc contains two silicate sheets, which consist of covalently bonded SiO_4 tetrahedra, see Fig. 2. Between the two silicate layers, magnesium (Mg^{2+}) and hydroxide (OH^-) ions are located, which bind the layers with ionic bonds. These quasi-2D layers are then stacked together with van der Waals forces forming bulk talc (not shown).

In our study we consider four types of erbium related defects: erbium substitutional defect at the magnesium sites ($Er_{Mg\text{-}1}$ and $Er_{Mg\text{-}2}$), erbium substitutional defect and hydrogen vacancy complex ($V_HEr_{Mg\text{-}x}$), erbium substitutional defect and two hydrogen vacancy complex ($2V_HEr_{Mg\text{-}x}$), and erbium interstitial defect (Er_i).

The magnesium sites, Mg_1 and Mg_2, see Fig. 2, can be substituted with transition metal impurities. This is supported by our previously work, [36] where we showed that the formation energy of a magnesium vacancy in talc is significantly lower than that of a silicon vacancy.

As erbium prefers cationic form (predominantly Er^{3+}) in nature, it is reasonable to assume that it also occupies the cationic position (i.e., the Mg^{2+} site) when applied as a dopant in talc. Two chemically nonequivalent Mg positions can be distinguished in talc. The two Mg types differ in their local bonding environments, as visualized in Fig. 2c. All Mg^{2+} ions are coordinated in an octahedral fashion, by two oxygens from OH^- ions and four oxygens from SiO_4 tetrahedrons. In talc strucutre there are two possibilities for the relative arrangement of the aforementioned six ligands. Mg_1 and Mg_2 represent the trans case (OH^- ions in opposite position, at $\approx 180°$ of HO-Mg-OH angle) and the cis case (OH^- ions in adjacent position, at $\approx 90°$ of HO-Mg-OH angle), respectively. Accordingly, Er_{Mg1} and Er_{Mg2} defects must be treated separately.

Although the hydroxyl groups of talc are not generally labile under ambient conditions, proton removal may become relevant under growth, irradiation, annealing, or charge-compensation conditions close to defects. This is consistent with the anisotropic surface chemistry of talc, where acid-base activity is mainly associated with edge sites rather than the basal planes, and with infrared studies showing proton migration and dehydroxylation upon heating.[62,63] We therefore consider Er_{Mg} complexes with one or two adjacent hydrogen vacancies (V_H), in addition to the hydroxyl-intact configuration.

Altogether, we arrive at a total of six erbium defect configurations studied in different charge states, summarized in Table 1. Different charge states result in different formal charge of the erbium cation, which fundamentally affects the optical properties (*vide infra*). Therefore, we put a specific emphasis on erbium charge in our nomenclature; for example, $V_H Er^{3+}_{Mg2}$ indicates a neutral defect, as the absence of an Mg^{2+} ion and a H^+ ion compensates the triple positive charge of Er^{3+}, see Table 1. Analogously, if the overall charge is positive or negative, one unit of charge is added ($V_H Er^{4+}_{Mg2}$) or removed ($V_H Er^{2+}_{Mg2}$) from Er, as the formal charge of main-group ions remains unaffected.

We further note that the overall spin quantum number (S) of the defect is solely determined by the charge state of the erbium cation, as indicated in Table 1.

Finally, in addition to the above 6 intralayer defects, we considered erbium impurities inter-

Table 1: List of erbium defects and charge states studied in this work. The nomenclature emphasizes the formal charge of erbium as well as the spin of the defects.

Mg site	# of V_H	Defect configuration	Charge state		
			q = 1	q = 0	q = -1
1	0	Er_{Mg1}	$\mathbf{Er^{3+}_{Mg1}}$ S = 3/2	$\mathbf{Er^{2+}_{Mg1}}$ S = 1	$\mathbf{Er^{+}_{Mg1}}$ S = 3/2
1	1	$V_H Er_{Mg1}$	$\mathbf{V_H Er^{4+}_{Mg1}}$ S = 2	$\mathbf{V_H Er^{3+}_{Mg1}}$ S = 3/2	$\mathbf{V_H Er^{2+}_{Mg1}}$ S = 1
1	2	$2V_H Er_{Mg1}$	$\mathbf{2V_H Er^{5+}_{Mg1}}$ S = 5/2	$\mathbf{2V_H Er^{4+}_{Mg1}}$ S = 2	$\mathbf{2V_H Er^{3+}_{Mg1}}$ S = 3/2
2	0	Er_{Mg2}	$\mathbf{Er^{3+}_{Mg2}}$ S = 3/2	$\mathbf{Er^{2+}_{Mg2}}$ S = 1	$\mathbf{Er^{+}_{Mg2}}$ S = 3/2
2	1	$V_H Er_{Mg2}$	$\mathbf{V_H Er^{4+}_{Mg2}}$ S = 2	$\mathbf{V_H Er^{3+}_{Mg2}}$ S = 3/2	$\mathbf{V_H Er^{2+}_{Mg2}}$ S = 1
2	2	$2V_H Er_{Mg2}$	$\mathbf{2V_H Er^{5+}_{Mg2}}$ S = 5/2	$\mathbf{2V_H Er^{4+}_{Mg2}}$ S = 2	$\mathbf{2V_H Er^{3+}_{Mg2}}$ S = 3/2

calated between two van der Waals-bound layers of talc (Er_i) as the 7th possible configuration.

Defect strucutres. After the geometry relaxation of pristine talc, the Mg-O bond lengths in the octahedral coordination environments of the Mg_1 and Mg_2 sites are approximately equal in all directions, and are determined to be $2.04 - 2.07$Å. The value of trans and cis O-Mg_1-O angles is $179° - 180°$ and $84° - 95°$, respectively. The deviation from the ideal octahedral angles $180°$ and $90°$ derive from the intrinsic asymmetry of the lattice.

Interestingly, the erbium-doped talc undergoes only minor structural modifications, see Fig. 2. Following Er incorporation to either Mg_1 or Mg_2 site, the metal-oxygen bond lengths generally increase to approximately 2.2Å - 2.3Å, albeit 1-2 out of the six Er-O bonds tends to slightly shrink to 2.01 - 2.04Å. We note that the variation in Er-O interatomic distances can be partly traced back

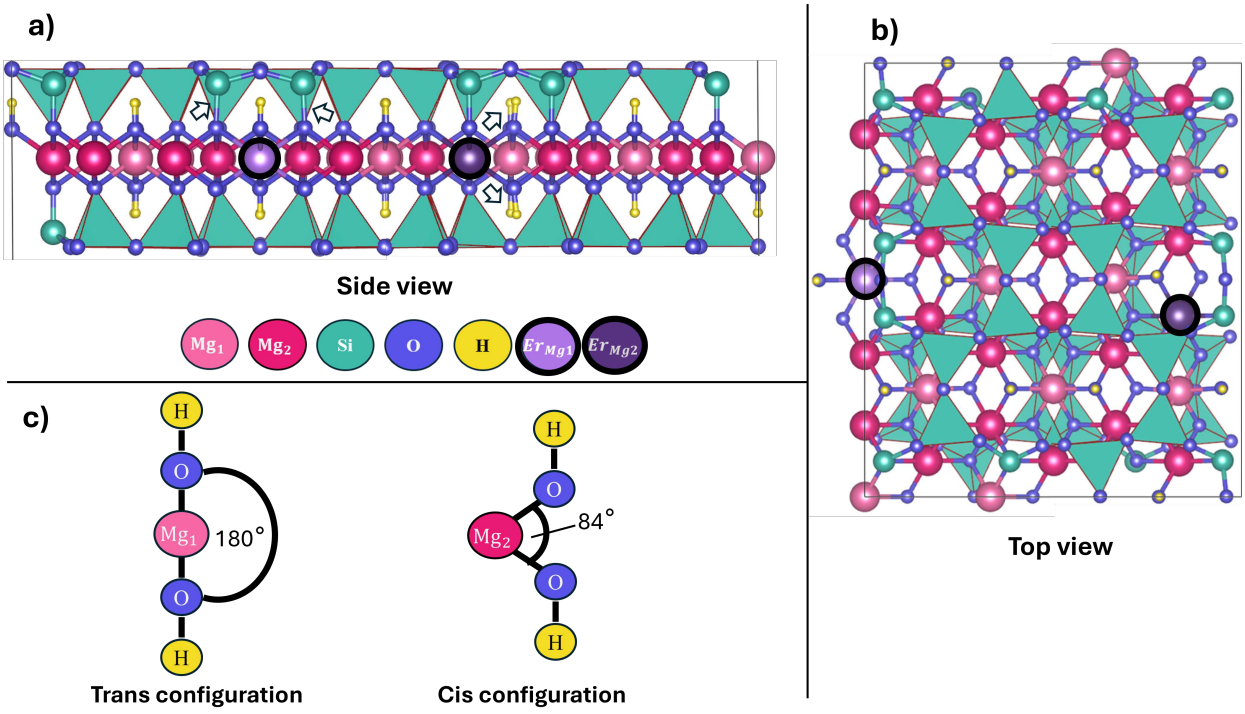

Figure 2: Structure of single-layer talc doped with Er atoms in a) side view, revealing two sheets of silicates (SiO_4) on the top and on the bottom of the structure, and b) in top view. For clarity, SiO_4 tetrahedra are filled with green color, while the position of individual Si atoms is only shown for selected sites. c) Visualization of the conceivable relative configurations of OH ligands in the coordination sphere of Mg_1 and Mg_2 atoms.

to the asymmetrically filled f orbitals. The metal-oxygen bond elongation is primarily driven by the larger ionic radius of erbium compared to magnesium.

The O-Er-O bond angles also cover a significantly wider range than the O-Mg-O angles of pristine talc. In particular, trans O-Er-O angles of as low as $170°$ are observed (the maximal value is still near $180°$), while the cis angle is also versatile ($82° - 98°$).

A further detectable geometrical change induced by Er_{Mg} substitution is the tilt of previously vertical Si-O bonds and OH groups, see white arrows in Fig. 2. These distortions, however, possess negligible influence on the electronic properties of the lattice.

Formation energy. Next, we study the formation energy (E^f) of the selected erbium related erbium-related defects. The formation energy of defect X in charge state q can be written as a function of the Fermi level (E_{F}) as [64]

$$E^f[X^q] = E_{\mathrm{tot}}[X^q] - E_{\mathrm{tot}}[\mathrm{bulk}] - \sum_i n_i \mu_i + qE_{\mathrm{F}} + E_{\mathrm{corr}}, \tag{1}$$

where $E_{\mathrm{tot}}[\mathrm{bulk}]$ is the total energy of the pristine talc supercell, $E_{\mathrm{tot}}[X^q]$ is the total energy of the defective talc supercell in charge q, while n_i is the signed number of added or removed atoms, which possess a chemical potential of μ_i in their most stable elementary form. Finally, E_{corr} stands for the charge correction term for $q \neq 0$ due to the periodic boundary condition. [65]

First, we investigate the stability of the interstitial positively charged erbium impurities, intercalated between the talcum layers (Er_i; see Supplementary Information, section **??**). We found that such defects are unlikely to be detectably present due to their large formation energy. Even under the most favorable p-type conditions, the formation obtained with the R2SCAN exchange correlation functional is close to 10 eV and rapidly increases with increasing Fermi energy. Therefore, we disregard Er_i type defects and consider only $\mathrm{Er}_{\mathrm{Mg}}$ related defects hereinafter.

Next, we discuss the formation energies of neutral $\mathrm{Er}_{\mathrm{Mg}}$ related configurations, which are summarized in Table 2. The R2SCAN formation energies are also compared with HSE06 results in Supplementary Note **??**, which show good agreement between the two methods. The obtained energies are remarkably low, reaching even negative values (from -0.5 to -3.3 eV), indicating that the incorporation of an erbium atom into a talc layer is energetically favourable. In addition, the calculated E^f values show that the difference in formation energies at Mg_1 and Mg_2 sites is minimal. Consequently, $\mathrm{Er}_{\mathrm{Mg1}}$ and $\mathrm{Er}_{\mathrm{Mg2}}$ substitutions are expected to appear simultaneously in talc.

As for non-neural charge states, the qE_F term in Eq. 1 varies in a wide interval, owing to the large band gap of talc[36]. Therefore, the formation energies can be further lowered under favorable circumstances, even by several electronvolts. This effect is visualized in Fig. 3, where E^f is depicted with respect to the Fermi level. At each E_F, only the minimal-energy charge state

Table 2: Neutral-charge formation energies (E^f) and charge transition levels (ϵ, given relative to the valence band maximum) of defect structures considered in our study. All values are obtained with the METAGGA R2SCAN level of theory in a single-layer talcum model. (*R2SCAN optimization for the charge-neutral structure failed. The provided values are estimations based on HSE06 test calculations, see SI, section **??**.)

Defects	E^f(q=0) (eV)	ϵ(+2/+1) (eV)	ϵ(+1/0) (eV)	ϵ(0/-1) (eV)
Er_{Mg1}	-1.6*	-0.2	5.8*	-
Er_{Mg2}	-1.6	-0.2	5.8	-
$V_{\mathrm{H}}Er_{\mathrm{Mg1}}$	-3.3	-	0.9	-
$V_{\mathrm{H}}Er_{\mathrm{Mg2}}$	-3.3	-	0.9	-
$2V_{\mathrm{H}}Er_{\mathrm{Mg1}}$	-0.9	-	-	2.5
$2V_{\mathrm{H}}Er_{\mathrm{Mg2}}$	-0.5		0.4	2.0

is shown.

Charge transition levels are calculated for all the considered defects using the formula[66] of

$$\epsilon(q|q') = \frac{E_{\mathrm{tot}}[X^q] + E_{\mathrm{corr}}(q) - (E_{\mathrm{tot}}[X^{q'}] + E_{\mathrm{corr}}(q'))}{q' - q} - \epsilon_{VBM} \tag{2}$$

where $E^f(X^q)$ is the formation energy of defect X in charge state q.

The computed values, including charge corrections, are provided in Table 2. Analyzing the position of the charge transition level with respect to the position of the band edge, the valence band maximum in our case, we can identify the stable charge states of the defects at a given value of the Fermi energy, see Fig. 3.

Conspicuously, while $V_{\mathrm{H}}Er_{\mathrm{Mg}}$ defects favor electroneutrality regardless of the Fermi level (except for extreme p-type conditions), the most stable charge state of Er_{Mg} and $2V_{\mathrm{H}}Er_{\mathrm{Mg}}$ is positive and negative, respectively. In the case of Er_{Mg}, the (+1/0) charge transition appears at n-type limit at 5.8 eV above the valence band edge, while E^f lowers to ≈ -7 eV at p-type talc when the Fermi

energy is close to the VBM. Furthermore, we find that the +2 charge state of Er_{Mg} is not stable in the band gap of talc, see Table 2. For $2V_HEr_{Mg}$, however, the (0/-1) charge transition occurs at intermediate E_F levels, making the neutral $q = 0$ state also relevant at weak p-type conditions. For semi-insulating and n-type samples, the negative charge state is stable. We also note that CTLs slightly depend on the position of Er in the lattice in the case of $2V_HEr_{Mg}$ configuration, see Fig. 3.

Based on Table 1 and Fig. 3, we can relate the most stable charge states to the formal charge of the erbium cation. Chemical intuition suggests the commonly observed Er^{3+} to be dominantly formed, which is corroborated by the above results. The positively charged Er_{Mg}, the neutral V_HEr_{Mg} and the negatively charged $2V_HEr_{Mg}$ defects all correspond to Er^{3+}, see Fig. 3. The Er^{3+}_{Mg} $V_HEr^{3+}_{Mg}$ and $2V_HEr^{3+}_{Mg}$ configurations are the stable ones for a Fermi energy positioned in the middle of the band gaps expected for pristine talc layers lacking intrinsic defects[36]. Notable alternative cationic forms of Er were found for neutral $2V_HEr_{Mg}$ (corresponding to Er^{4+} ion at the center), and - at the extreme limits of E_F - for neutral Er_{Mg} (Er^{2+} center), for positively charged V_HEr_{Mg} (Er^{4+} center) and for positively charged $2V_HEr_{Mg}$ (Er^{5+} center).

Kohn-Sham electronic structure of the most stable defects. Next, we discuss the electronic structure and the optical properties of the erbium defect forms found to be stable at Fermi levels lying within the band gap (Er^{2+}_{Mg}, Er^{3+}_{Mg}, $V_HEr^{3+}_{Mg}$, $V_HEr^{4+}_{Mg}$,$2V_HEr^{3+}_{Mg}$, $2V_HEr^{4+}_{Mg}$, and $2V_HEr^{5+}_{Mg}$), at both possible Mg positions.

The single-determinant (Kohn-Sham) electronic structure of the most stable erbium-containing defects is shown in Fig. 4. For the case of Er^{3+}_{Mg}, the position of conduction and valence band orbitals closely resembles the Kohn-Sham structure of the bulk talc (see green bands), while for V_H containing cases the valence band edge can be shifted upward by 1-2 eV due to the perturbation of the narrow, large density of states oxygen related valnece band, which shows high susceptibility for the pertubation of oxigen occupany[36].

In the band gap, only three (four) empty spin-down orbitals can be found for Er^{3+} (Er^{4+}), which correspond to the unoccupied $4f$ atomic orbitals of Er affected by a small degree of hybridization. The remaining $4f$ orbitals are situated deep inside the valence band.

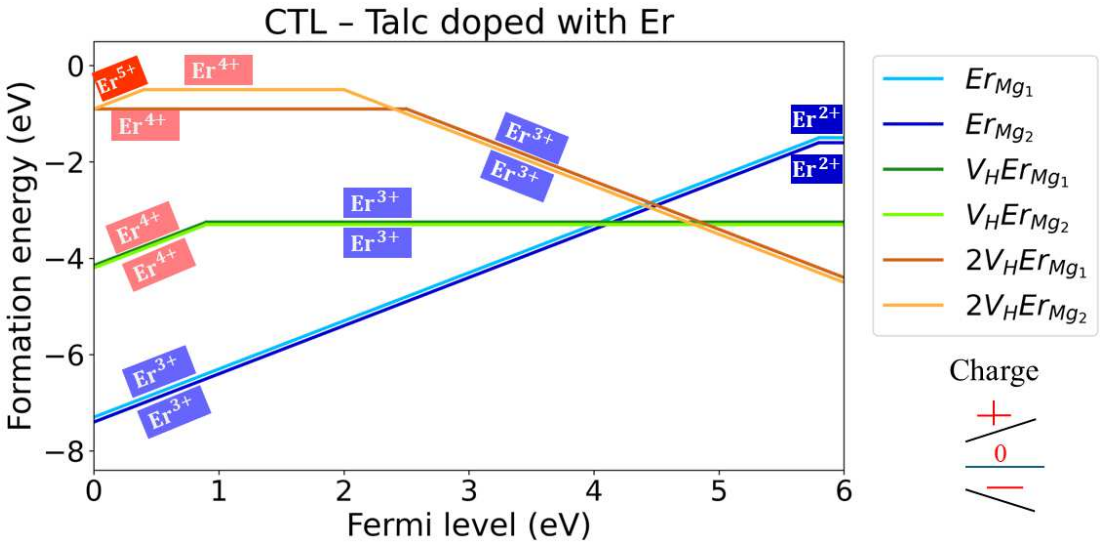

Figure 3: Formation energy of erbium defects as a function of the Fermi level ($E_F = 0$ corresponds to the valence-band maxiumum.)

It is interesting to compare the arrangement of the aforementioned empty $4f$ orbitals to the structure of free erbium cations in vacuum. If Mg_1 or Mg_2 is substituted by Er^{3+} in monolayer talc (Er^{3+}_{Mg}, $V_HEr^{3+}_{Mg}$, and $2V_HEr^{3+}_{Mg}$), the cristal field induces orbital splitting only 6-8 times larger than that of the free Er^{3+} ion. The splitting of the empty $4f$ orbitals reaches 0.15-0.25 eV, depending on the configuration. This result for Er^{3+}_{Mg}, $V_HEr^{3+}_{Mg}$ and $2V_HEr^{3+}_{Mg}$ implies that such systems can be interpreted as practically free Er^{3+}, i.e. no $4f$ related bonds are formed. By contrast, the $4f$ orbitals of Er^{4+} defects ($V_HEr^{4+}_{Mg}$ and $2V_HEr^{4+}_{Mg}$) cover an energy range of 1.6-2.2 eV, which are 15 - 20 times larger than that of the splitting of the free Er^{4+} ion, indicating significant interaction between the ion and the surrounding ligands. This enhanced susceptibility to the ligand field, which can presumably be traced back to the higher effective nuclear charge of Er^{4+} acting on the neighboring oxygen atoms, is also manifested in the Mg site dependence of orbital energy levels. In particular, for $2V_HEr^{4+}_{Mg1}$, a significantly smaller energy separation is observed (1.64 eV) than for $2V_HEr^{4+}_{Mg2}$ (2.15 eV).

Optical properties of Er^{3+}_{Mg} and Er^{4+}_{Mg} defects. The ${}^4I_{13/2} \rightarrow {}^4I_{15/2}$ optical transition of Er^{3+} can be modeled by WFT, in the framework of quasi-degenerate perturbation theory (QDPT) [67]. At first, we generate 13 spin-free eigenstates (the I states are 2L+1=13-fold degenerate) in a complete active space - self-consistent field (CASSCF) calculation [68], see Methods and Supplementary Note **??** for details. By introducing spin-orbit coupling (SOC), these 13 states are split into 13×4=52 coupled basis states. The linear combination of this basis states gives the proper wavefunction of the individual, (2J+1)-fold degenerate spin-orbit coupled eigenstates of ${}^4I_J$. We note that the transition for the Er^{4+} ion, which has 10 electrons and 4 holes on its f orbitals corresponding to $S = 2$ and $L = 6$, is ${}^5I_7 \rightarrow {}^5I_8$.

In free Er^{3+} and Er^{4+} ions, the (2J+1)-fold degeneracy of spin-orbit coupled sublevels is exact, and the optical transition is only allowed by a weak magnetic dipole moment (μ_M). In this case, the radiative rate ($k_{PL,M}$) can be calculated as

$$k_{\mathrm{PL,M}} = \frac{1}{\tau_{PL,M}} = \sum_{if} p_i \frac{n^3 \Delta E_{if}^3}{3\pi\varepsilon_0 \hbar^4 c^5} \left|\mu_{M,if}\right|^2, \tag{3}$$

where ΔE_{if} is the energy gap between the initial (i) and final (f) spin-orbit coupled eigenstate and

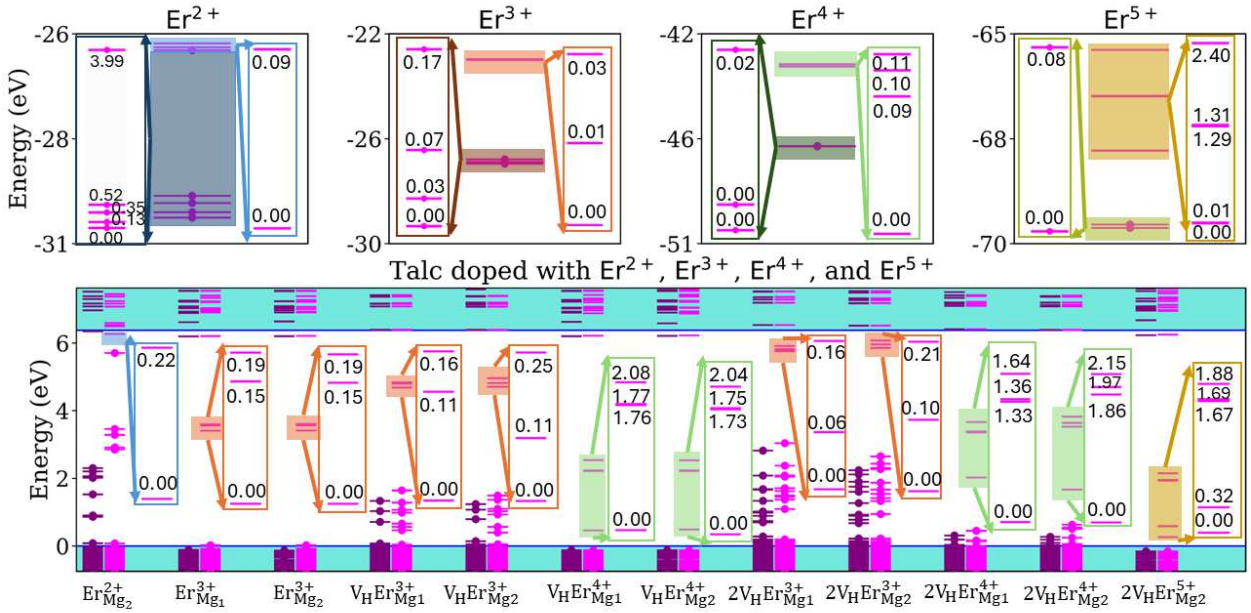

Figure 4: Kohn-Sham electronic structure of the thermodynamically most stable erbium impurities in talc, compared to the 4f subshell of free erbium cations (upper row of diagrams). Purple and pink lines represent spin-up and spin-down channells, respectively, while circles indicate occupation by an electron. Bottom and top green regions indicate the valence and conduction band of talc, respectively.

p_i is the Boltzmann factor of the initial state. We recall that the number of possible if combinations is $(2J_i + 1)(2J_f + 1)$.

To obtain reference values for studying the erbium ions in talc, we first modeled the emission rate for Er^{3+} and Er^{4+} in vacuum (refractive index: n = 1). The results are shown in the corresponding rows of Table 3, where we gathered the energy difference related to J quantum number change (ΔE), a Boltzmann-averaged representative magnetic dipole (μ_M, see also in Supplementary Information section **??** for the details of Boltzmann statistics) and the lifetime of emission (τ_{PL}).

It can be observed that a photon energy of 0.75 eV was obtained for free Er^{3+} using our WFT protocol, which is in good agreement with the experimental observation of 1550 nm (0.80 eV). Moreover, the radiative lifetime of 121 ms is consistent with $4f^n$-specific intermediate coupling calculations [69], which gave 98 ms for the same transition. As for Er^{4+}, the transition was found to occur with comparable characteristics, albeit with a slightly lower photon energy (0.63 eV, or 1970 nm) and also a lower rate (162 ms lifetime).

In the next step, we discuss the effect of the crystal field of the embedding talc lattice on these characteristic emissions. Firstly, due to the presence of the external crystal field, states of equal J quantum numbers lose their degeneracy and are split into Stark components. Consequently, multiple peaks are expected in the photoluminescence spectrum, lying in an energy range of 30-120 meV of width (considering an intensity cutoff of 95%). Furthermore, the weighting by p_i in Eq. 3 cannot be substituted by a simple arithmetic averaging anymore, and the results become sensitive to temperature. In this work, we characterized the emission at room temperature (300 K).

Secondly, $k_{\mathrm{PL,M}}$ scales with the third power of the refractive index, therefore, the talc environment with n=1.55 significantly accelerates the emission. $k_{\mathrm{PL,M}}$ can also be altered due to an environment-induced change in the $\mu_{M,if}$ terms, however, the sign of this effect cannot be predicted *a priori*.

Thirdly, the electric dipole moment (μ_E) can also arise in the lattice, which contributes to the

PL rate as

$$k_{\mathrm{PL,E}} = \frac{1}{\tau_{PL,E}} = \sum_{if} p_i \frac{n\Delta E_{if}^3}{3\pi\varepsilon_0\hbar^4 c^3} \left|\mu_{E,if}\right|^2 \tag{4}$$

producing an overall half-life of

$$\tau_{\mathrm{PL}} = \frac{1}{k_{PL,M} + k_{PL,E}}. \tag{5}$$

The results obtained for Er^{3+} and Er^{4+} ions, substituted to the Mg_1 or Mg_2 site of talc, are also provided in Table 3. Apart from the characteristics discussed for free ions, we also present here the Boltzmann-averaged representative transition dipole moment (μ_E) and the contribution of the electric and magnetic terms to the overall rate in percentage (M% and E%).

Since we have already observed the vast robustness of the Kohn-Sham structure of Er^{3+} against crystal field effects, it is not surprising to see that all talc-embedded Er^{3+} systems share practically the same optical lifetime (27-31 ms) for ${}^4I_{13/2} \rightarrow {}^4I_{15/2}$ relaxation. The enhanced rate of photoemission relative to the parent ion (τ_{PL}=121 ms) can almost solely be traced back to the introduction of the lattice refractive index (n = 1.55) to the $k_{\mathrm{PL,M}}$ term, which gives a factor of $1.55^3 \approx 3.7$. Compared to this effect, the crystal field-induced change in the magnetic transition dipole moment (from 1.17 to 1.21-1.24 μ_B) can be considered as insignificant. As a secondary effect, the appearance of a small (< 0.01 Debye) electric transition dipole moment also contributes to the reduction of the radiative lifetime. For $V_H Er_{Mg}^{3+}$ and $2V_H Er_{Mg}^{3+}$ defects, we observe approximately an order of magnitude increase of the electric transition dipole moment. As a consequence, the contribution of the electric dipole-driven transition rate increases to 11%-15%, which, however, showcases that the magnetic dipole transition still dominates. An exception to this trend is the $2V_H Er_{Mg1}^{3+}$ configuration, where, due to the trans configuration of the hydrogen vacancies, see Fig. 2, the V_H induced electric field perturbations cancel out to a large degree, see Table 3.

In the case of the ${}^5I_7 \rightarrow {}^5I_8$ emission in Er^{4+}, the crystal field effects are more prevalent, as expected from f-orbital splittings seen in the Kohn-Sham orbital picture in Fig. 4. We observe in Table 3 that the talc environment considerably enhances the magnetic transition dipole moment. While μ_M=1.30 μ_B was calculated for the free ion, $2V_H Er_{Mg1}^{4+}$ shows a 1.5-fold enhancement (μ_M=1.9 μ_B). The Stark splitting is also more significant, as a result of which a broader range

of ZPL energies appear (ZPLs of as low as 0.56 eV and as high as 0.68 eV appear, compared to the free-ion ZPL of 0.63 eV), the higher end of which further reduces the lifetime. These effects, combined with the refractive index-related acceleration factor ($n^3 \approx 3.7$) result in lifetimes of 29-36 ms. We note that the similarity to Er^{3+} lifetimes, despite the aforementioned emission-facilitating crystal field effects, can be traced back to the longer-living parent ion (Er^{4+}, with $\tau_{PL} = 162$ ms).

Altogether, the primary effect of the talc lattice is the facilitation of the magnetic dipole induced photoluminescence ($k_{PL,M}$) of the embedded Er^{3+} and Er^{4+} ions via its refractive index. In the case of Er^{3+} and Er^{4+}, additional non-negligible effects arise from the enhancement of the electric transition dipole and the enhancement of the magnetic transition dipole, respectively, further decreasing the a radiative lifetime compared to the free ion. The obtained lifetimes fall in the range of 29-36 ms, which is commensurable to those measured experimentally in Er^{3+}-doped crystals reported in the literature [17,41,45,49,58–61]. Therefore, based on our results, the natural 2D-structured lattice of talc can be considered as a promising host for quantum technological applications of Er^{3+} and Er^{4+} photoemission lines.

To evaluate the performance of talc-embedded Er centers regarding quantum applications, where a single ZPL, i.e., one selected Stark transition, is targeted, we gathered the brightest expected single-photon emission channels in Table 4. We also assigned the magnetic sublevel (M_J quantum number) to the initial and final Stark states involved in the selected optically favorable transition, even though we emphasize that presence of the crystal field inevitably mixes the free-ion-like M_J sublevels and the unequivocal identification is therefore not always possible. As expected, the maximal accessible single-photon rates - without Boltzmann weighting of the initial state- lie in the order of magnitude of the total PL rate (40-80 ms, see SI for details). Such slow optical decay is obviously inappropriate for practical single-photon-source operation and, therefore, any selected ZPL would have to be enhanced by optical engineering, most naturally by exploiting the Purcell effect. In this regard, however, talc has advantageous features: as an exfoliable van der Waals silicate, it should be compatible with heterogeneous integration onto pre-fabricated dielectric or plasmonic nanophotonic structures, allowing the Er^{3+} center to be placed in the near field of an optical resonator without aggressive nanofabrication of the host crystal itself. Analogous strate-

Table 3: Optical properties of talc-embedded Er centers from the point of view of **general telecom-band optoelectric applications** (i.e. the total radiative decay involving all Stark transitions is investigated). Energy difference range (ΔE), representative magnetic transition dipole moment (μ_M), representative electric transition dipole moment (μ_E), radiative lifetime (τ_{PL}) and the contribution ratio of magnetic-iduced ($M\%$) and electric-induced ($E\%$) emission, calculated for the $^4I_{13/2} \rightarrow^4 I_{15/2}$ transition of Er^{3+} and the $^4I_7 \rightarrow^4 I_8$ transition of Er^{4+} at WFT level.

System	ΔE [eV]	μ_M [μ_B]	μ_E [D]	τ_{PL} [ms]	M%	E%
Free Er^{3+}	0.75	1.17	-	121	100%	-
Talc, Er^{3+}_{Mg1}	0.73-0.76	1.22	0.00046	31	99.9%	0.1%
Talc, Er^{3+}_{Mg2}	0.73-0.76	1.22	0.00098	31	99.7%	0.3%
Talc, $V_H Er^{3+}_{Mg1}$	0.73-0.78	1.21	0.00725	27	85.1%	14.9%
Talc, $V_H Er^{3+}_{Mg2}$	0.73-0.78	1.21	0.00663	28	87.4%	12.6%
Talc, $2V_H Er^{3+}_{Mg1}$	0.73-0.77	1.24	0.00024	31	100.0%	0.0%
Talc, $2V_H Er^{3+}_{Mg2}$	0.73-0.78	1.21	0.00600	29	89.3%	10.7%
Free Er^{4+}	0.63	1.30	-	162	100%	-
Talc, $2V_H Er^{4+}_{Mg1}$	0.56-0.68	1.94	0.00044	29	100.0%	0.0%
Talc, $2V_H Er^{4+}_{Mg2}$	0.58-0.66	1.45	0.00629	36	91.7%	8.3%

gies have already been demonstrated for hBN single-photon emitters coupled to photonic-crystal and microring cavities and, more directly for rare-earth systems [70–76].

Discussion

The present results establish talc as a previously unexplored rare-earth host that combines favorable defect thermodynamics with optical characteristics relevant for telecom photonics and quantum technologies. In contrast to many conventional Er-doped materials, talc provides a naturally layered van der Waals lattice that can be mechanically exfoliated down to single layer level? and integrated into hybrid photonic architectures? without the need for epitaxial growth. The calculated formation energies indicate that substitutional incorporation of erbium is energetically favor-

Table 4: Optical properties of talc-embedded Er centers from the point of view of **quantum applications**, i.e., the highest radiative decay rate among all Stark transitions is investigated). Energy difference (ΔE), initial (M_{J_i}) and final (M_{J_f}) J sublevels, magnetic transition dipole moment (μ_M), and electric transition dipole moment (μ_E).

System	ΔE [eV]	M_{J_i}	M_{J_f}	μ_M [μ_B]	μ_E [D]
Talc, $Er^{3+}{}_{\text{Mg1}}$	0.75	$\pm 13/2$	$\pm 13/2$	0.91	0.00016
Talc, $Er^{3+}{}_{\text{Mg2}}$	0.75	$\pm 13/2$	$\pm 13/2$	0.93	0.00018
Talc, $V_H Er^{3+}{}_{\text{Mg1}}$	0.73	$\pm 13/2$	$\pm 15/2$	0.98	0.00342
Talc, $V_H Er^{3+}{}_{\text{Mg2}}$	0.73	$\pm 13/2$	$\pm 15/2$	0.99	0.00315
Talc, $2V_H Er^{3+}{}_{\text{Mg1}}$	0.76	$\pm 5/2$	$\pm 7/2$	1.04	0.00007
Talc, $2V_H Er^{3+}{}_{\text{Mg2}}$	0.75	$\pm 13/2$	$\pm 15/2$	1.05	0.00244
Talc, $2V_H Er^{4+}{}_{\text{Mg1}}$	0.68	± 7	± 8	1.05	0.00009
Talc, $2V_H Er^{4+}{}_{\text{Mg2}}$	0.66	± 3	± 4	0.87	0.00366

able and should occur readily under suitable synthesis or diffusion conditions. Importantly, the preferred charge states correspond predominantly to Er^{3+}, ensuring access to the technologically important ${}^4I_{13/2} \rightarrow {}^4I_{15/2}$ transition near 1.55 μm.

A key observation is that the talc crystal field perturbs the Er 4f shell only weakly in the Er^{3+} configuration. Consequently, the telecom transition largely retains its free-ion character, while the local symmetry generates Stark splitting that provides multiple spectrally resolvable optical transitions. This combination is particularly attractive for quantum photonics because it enables narrow optical lines while preserving the exceptional robustness of rare-earth 4f states. The calculated radiative lifetimes of approximately $\sim$30 ms fall within the range reported for established rare-earth photonic hosts, suggesting that the talc environment does not compromise the desirable optical properties of erbium.

From a device perspective, the most significant advantage of talc may arise from its compatibility with heterogeneous integration. Exfoliated talc flakes containing Er centers could be

transferred onto pre-fabricated photonic-crystal cavities, microring resonators, dielectric metasurfaces, or plasmonic nanostructures. Such an approach avoids aggressive nanofabrication of the host crystal itself while still enabling large Purcell factors and efficient control of selected Stark transitions. Similar integration strategies have proven highly successful for other van der Waals quantum emitters and could provide a realistic route toward telecom single-photon sources based on erbium centers in talc.

The natural two-dimensional character of talc also opens opportunities beyond isolated emitters. Layered erbium-doped talc could be incorporated into van der Waals heterostructures together with graphene, hexagonal boron nitride, transition-metal dichalcogenides, or lithium-niobate-on-insulator photonic circuits. Such hybrid platforms may enable optical modulation, electrical tuning, and cavity-enhanced readout of rare-earth states while preserving the scalability associated with layered materials. Because talc possesses atomically flat, chemically inert surfaces and a wide band gap, it is expected to introduce minimal optical loss and limited background luminescence.

Regarding fabrication, several experimentally accessible routes seem feasible. Er incorporation may be achieved during growth, through ion implantation followed by thermal annealing, or via diffusion-assisted doping protocols already established for rare-earth ions in oxides and silicates. The large thermodynamic driving force predicted here suggests that stable substitutional configurations should form readily once Er reaches Mg lattice sites. Future experimental work should clarify achievable concentrations, optical linewidths, spectral diffusion characteristics, and spin coherence properties.

Overall, our results suggest a broader perspective for naturally occurring layered silicates that represent a largely unexplored family of quantum-photonic materials. Within this emerging class, erbium-doped talc appears as a particularly promising candidate that combines telecom-band emission, defect stability, and van der Waals integrability. These features position it as a potentially attractive platform for future integrated quantum-photonic technologies.

Methods

In this work, both density functional theory and wavefunction theory were used to study the properties of Er-doped talc. Computational details are given below, while input files and optimized geometries are provided in sections **??** and **??** of the Supplementary Information, respectively.

Density functional theory on supercells. To investigate formation energies and Kohn-Sham electronic structures, we employ density functional theory calculations in periodic boundary conditions as implemented in the Vienna Ab initio Software Package (VASP, version is VASP/5.4.4)[77,78]. For the present work, the R2SCAN[79] density functional is selected, which is computationally less demanding than the widely applied hybrid functional of HSE06[80–82]. Our test calculations, detailed in section **??** of the Supplementary Information, revealed that R2SCAN sufficiently reproduces the HSE06-level geometries and formation energies of Er centers. To account for the weak van der Waals interaction between the layers, the Grimme-D3 correction[83] is applied on top of R2SCAN. Unless indicated otherwise, single-layer talc supercells of 3×2 size (containing 252 atoms) are used, with only Gamma-point sampling of the Brillouin zone.

Kohn-Sham wavefunctions of the valence electrons are expanded in a plane wave basis set of 440 eV. We use the projector-augmented wave (PAW) method[84] to describe the potential of the nucleus and the weakly interacting core electrons of the atoms. A vacuum spacing of 9 Å is introduced into the simulation cell to minimize van der Waals interactions between neighboring periodic supercells. Furthermore, to accurately describe the 4f shell, we turn on non-spherical exchange-correlation contributions inside the PAW augmentation spheres. The stopping criteria for the electronic self-consistent field (SCF) loop and the structural relaxation are $\Delta E < 10^{-6}$ eV and $F_i < 10^{-3}$ eV/Å, where ΔE is the change of the total energy in an iteration of the SCF loop, and F_i is the length of the force vector acting on atom i.

Wavefunction theory on cluster models. The description of initial and final spin-obit coupled states of Er^{3+} and Er^{4+} photoluminescence lines requires multideterminantal wavefunction theory, which is, however, only available for cluster models in conventional quantum chemical software. Herein, based on the work of Tunega and Turi Nagy [85], we construct hydrogen terminated clusters

containing $298 - n_{V_H}$ atoms, where n_{V_H} is the number of hydrogen vacancy sites. A more detailed description and the visualization of these models is provided in the Supplementary Information under section **??**. The position of atoms (with the exception of the terminating hydrogens) were taken from DFT-optimized supercell geometries.

To confirm that the finite size of the cluster does not introduce any artifacts, we compared the local electrosctatic potential in the vicinity of the Er dopant in the cluster and in the supercell at the same level of theory and found no significant differences (see section **??** of the Supplementary Information).

Wave-function-theory (WFT) calculations were carried out using the ORCA 6.1.0 program package[86–88]. Static correlation within the open 4f shell was treated at the state-averaged complete active space self-consistent field (SA-CASSCF) level[89]. The active space comprised seven active orbitals, corresponding to the 4f subshell of Er, which were selected from initial DFT orbitals, transformed by the atomic valence active space (AVAS) method[90]. The number of active electrons was chosen according to the formal oxidation state of the erbium ion: CAS(11,7) and CAS(10,7) were used for Er^{3+} ($4f^{11}$ configuration) and Er^{4+} ($4f^{10}$ configuration), respectively. In both cases, 13 spin-free CASSCF roots were requested, corresponding to the $(2L+1) = 13$ components of the I term ($L = 6$). The spin multiplicity was set to quartet for Er^{3+} and quintet for Er^{4+}, consistent with the ${}^4I$ and ${}^5I$ ground terms, respectively.

On the basis of the obtained spin-free CASSCF eigenstates, spin–orbit coupled states were calculated within the quasi-degenerate perturbation theory (QDPT) framework for multireference spin-Hamiltonian calculations[67,91–93]. In this approach, the spin–orbit coupling (SOC) and spin–spin coupling (SSC) operators are represented in the basis of the non-relativistic CASSCF roots Ψ_I and their spin sublevels. The effective QDPT matrix can be written as

$$\left\langle \Psi_I^M \middle| \hat{H}_{CASSCF} + \hat{H}_{SOC} + \hat{H}_{SSC} \middle| \Psi_J^{M'} \right\rangle = \delta_{IJ}\delta_{MM'}E_I + \left\langle \Psi_I^M \middle| \hat{H}_{SOC} + \hat{H}_{SSC} \middle| \Psi_J^{M'} \right\rangle \tag{6}$$

where I and J label the CASSCF roots, while M and M' denote the spin sublevels. Although the

spin-sublevel dependence is not explicit in the spin-free CASSCF roots, it is introduced through Clebsch-Gordan coefficients according to the Wigner-Eckart theorem [92,94]. The SOC matrix elements were evaluated using the spin-orbit mean-field (SOMF) approximation [95,96]. Finally, E_I^{CASSCF} denotes the spin-free electronic energy of the Ith CASSCF root.

Diagonalization of the QDPT matrix yields the spin-orbit coupled eigenstates and the corresponding relativistic energy levels. The resulting multiplet structure was assigned to effective J quantum numbers by inspecting the quasi-degeneracies in the energy spectrum, as described in SI, section **??**.

For all CASSCF-QDPT calculations, the def2-SVP basis set was used together with the corresponding effective core potential (ECP) for Er [97–99]. Density fitting approximations were applied to accelerate the calculations, using the def2/J and def2-SVP/C auxiliary basis sets in the Coulomb and correlation auxiliary-basis slots, respectively [100–102].

Data availability

The main data supporting the findings of this study are available in the paper and its Supplementary Information. Further numerical data are available from the authors upon reasonable request.

Acknowledgements

G.D. is grateful to Laura Dolecsekné Mócsán for her assistance in constructing the impurity-doped talc structures, selecting the color scheme, and preparing the geometric illustrations. Z.B. acknowledges the financial support of the János Bolyai Research Fellowship of the Hungarian Academy of Sciences. We acknowledge the support of the European Union under Horizon Europe for the QRC-4-ESP project (Grant Agreement 101129663) and the QUEST project (Grant Agreement 101156088). N.T.S. acknowledges the EU project QuSPARC (Grant No. 101186889), the Vinnova projects (2025-03848, and QUASIC within QSIP, grant 2024-03597), and the EU via the Swedish Agency for Economic and Regional Growth (20370271). The computations were enabled by resources provided by the National Academic Infrastructure for Supercomputing in Sweden (NAISS) and the Swedish National Infrastructure for Computing (SNIC) at NSC, partially

funded by the Swedish Research Council through grant agreements no. 2022-06725 and no. 2018-05973. We acknowledge the Digital Government Development and Project Management Ltd. for awarding us access to the Komondor HPC facility based in Hungary

Competing interests

The authors declare no competing interests.

Author contributions

G.D. and Z.B. carried out the DFT and WFT calculations, respectively. G.D., Z.B., N.T.S. and V.I. analysed the data. G.D., Z.B., and V.I. wrote the manuscript with inputs from all coauthors. The work was supervised by Z.B. and V.I.

1. Balaram, V. Rare earth elements: A review of applications, occurrence, exploration, analysis, recycling, and environmental impact. *Geoscience Frontiers* **10**, 1285–1303 (2019).

2. Bünzli, J.-C. G. & Piguet, C. Taking advantage of luminescent lanthanide ions. *Chemical Society Reviews* **34**, 1048–1077 (2005).

3. Eliseeva, S. V. & Bünzli, J.-C. G. Lanthanide luminescence for functional materials and bio-sciences. *Chemical Society Reviews* **39**, 189–227 (2010).

4. Snitzer, E. Optical maser action of nd+3 in a barium crown glass. *Physical Review Letters* **7**, 444–446 (1961).

5. Mears, R. J., Reekie, L., Jauncey, I. M. & Payne, D. N. Low-noise erbium-doped fibre amplifier operating at 1.54 μm. *Electronics Letters* **23**, 1026–1028 (1987).

6. Bünzli, J.-C. G. Lanthanide luminescence for biomedical analyses and imaging. *Chemical Reviews* **110**, 2729–2755 (2010).

7. Auzel, F. Upconversion and anti-stokes processes with f and d ions in solids. *Chemical Reviews* **104**, 139–173 (2004).

8. Dibos, A. M., Raha, M., Phenicie, C. M. & Thompson, J. D. Atomic source of single photons in the telecom band. *Physical Review Letters* **120**, 243601 (2018).

9. Zhong, T. *et al.* Optically addressing single rare-earth ions in a nanophotonic cavity. *Physical Review Letters* **121**, 183603 (2018).

10. Yang, L., Wang, S., Shen, M., Xie, J. & Tang, H. X. Controlling single rare earth ion emission in an electro-optical nanocavity. *Nature Communications* **14**, 1718 (2023).

11. Ourari, S. *et al.* Indistinguishable telecom band photons from a single er ion in the solid state. *Nature* **620**, 977–981 (2023).

12. Yu, Y. *et al.* Frequency tunable, cavity-enhanced single erbium quantum emitter in the telecom band. *Physical Review Letters* **131**, 170801 (2023).

13. Uysal, M. T. *et al.* Spin-photon entanglement of a single ion in the telecom band. *Physical Review X* **15**, 011071 (2025).

14. Kimiaee Asadi, F. *et al.* Quantum repeaters with individual rare-earth ions at telecommunication wavelengths. *Quantum* **2**, 93 (2018).

15. Ortu, A., Holzäpfel, A., Etesse, J. & Afzelius, M. Storage of photonic time-bin qubits for up to 20 ms in a rare-earth doped crystal. *npj Quantum Information* **8**, 29 (2022).

16. Ruskuc, A. *et al.* Multiplexed entanglement of multi-emitter quantum network nodes. *Nature* **639**, 54–59 (2025).

17. Miniscalco, W. J. Erbium-doped glasses for fiber amplifiers at 1500 nm. *Journal of Lightwave Technology* **9**, 234–250 (1991).

18. Bader, J., Arianfard, H., Peruzzo, A. & Castelletto, S. Analysis, recent challenges and capabilities of spin-photon interfaces in silicon carbide-on-insulator **1**, 29. URL https://www.nature.com/articles/s44310-024-00031-8.

19. García-Arellano, G. *et al.* Erbium-implanted WS2 flakes with room-temperature photon emission at telecom wavelengths. *Nano Letters* (2025).

20. Seth, S. K. *et al.* Spin decoherence dynamics of Er3+ in CeO2 films. *Physical Review Letters* **135**, 266901 (2025).

21. Früh, J. Spectral stability of cavity-enhanced single-photon emitters in silicon **7**.

22. Le Dantec, M. *et al.* Twenty-three–millisecond electron spin coherence of erbium ions in a natural-abundance crystal **7**, eabj9786 (2021). URL https://www.science.org/doi/10.1126/sciadv.abj9786.

23. Gritsch, A., Ulanowski, A., Pforr, J. & Reiserer, A. Optical single-shot readout of spin qubits in silicon. *Nature Communications* **16**, 64 (2025).

24. Lyasota, A. *et al.* Narrow magneto-optical transitions of erbium implanted into silicon carbide-on-insulator **7**, 154. URL https://www.nature.com/articles/s43246-026-01154-5.

25. Gohari Kamel, N. *et al.* Erbium-doped fiber quantum memory for chip-integrated quantum-dot single photons at 980 nm (2026). URL https://www.nature.com/articles/s41534-026-01316-w.

26. Novoselov, K. S. *et al.* Two-dimensional gas of massless dirac fermions in graphene. *Nature* **438**, 197–200 (2005). URL http://dx.doi.org/10.1038/nature04233.

27. Wang, Q. H., Kalantar-Zadeh, K., Kis, A., Coleman, J. N. & Strano, M. S. Electronics and optoelectronics of two-dimensional transition metal dichalcogenides. *Nature nanotechnology* **7**, 699–712 (2012).

28. Geim, A. K. & Grigorieva, I. V. Van der waals heterostructures. *Nature* **499**, 419–425 (2013).

29. Schaibley, J. R. *et al.* Valleytronics in 2d materials. *Nature Reviews Materials* **1**, 1–15 (2016).

30. Glavin, N. R. *et al.* Emerging applications of elemental 2d materials. *Advanced Materials* **32**, 1904302 (2020).

31. Turunen, M. *et al.* Quantum photonics with layered 2d materials. *Nature Reviews Physics* **4**, 219–236 (2022).

32. Parto, K. *et al.* Cavity-enhanced 2d material quantum emitters deterministically integrated with silicon nitride microresonators. *Nano Letters* **22**, 9748–9756 (2022).

33. Tran, T. T., Bray, K., Ford, M. J., Toth, M. & Aharonovich, I. Quantum emission from hexagonal boron nitride monolayers. *Nature Nanotechnology* **11**, 37–41 (2016).

34. Gottscholl, A. *et al.* Initialization and read-out of intrinsic spin defects in a van der waals crystal at room temperature. *Nature Materials* **19**, 540–545 (2020).

35. Frisenda, R., Niu, Y., Gant, P., Muñoz, M. & Castellanos-Gomez, A. Naturally occurring van der waals materials. *npj 2D Materials and Applications* **4**, 38 (2020).

36. Dolecsek, G., Bulancea-Lindvall, O., Davidsson, J. & Ivády, V. Native defects and impurities in talcum quasi-2d layers. *npj 2D Materials and Applications* **9**, 97 (2025).

37. Alencar, A. B., Barboza, A. P. M., Archanjo, B. S., Chacham, H. & Neves, B. R. A. Experimental and theoretical investigations of monolayer and few-layer talc. *2D Materials* **2**, 015004 (2015).

38. Harvey, A. *et al.* Exploring the versatility of liquid phase exfoliation: producing 2d nanosheets from talcum powder, cat litter and beach sand. *2D Materials* **4**, 025054 (2017).

39. Barcelos, I. D. *et al.* Infrared fingerprints of natural 2d talc and plasmon–phonon coupling in graphene–talc heterostructures. *ACS Photonics* **5**, 1912–1918 (2018).

40. Vahala, K. J. Optical microcavities. *Nature* **424**, 839–846 (2003).

41. Carnall, W. T., Goodman, G. L., Rajnak, K. & Rana, R. S. A systematic analysis of the spectra of the lanthanides doped into single crystal LaF3. *The Journal of Chemical Physics* **90**, 3443–3457 (1989).

42. Bünzli, J.-C. G. & Eliseeva, S. V. Basics of lanthanide photophysics. In Hänninen, P. & Härmä, H. (eds.) *Lanthanide Luminescence: Photophysical, Analytical and Biological Aspects*, Springer Series on Fluorescence, 1–45 (Springer, Berlin, Heidelberg, 2010).

43. Desurvire, E. & Simpson, J. R. Evaluation of $^4I_{15/2}$ and $^4I_{13/2}$ stark-level energies in erbium-doped aluminosilicate glass fibers. *Optics Letters* **15**, 547–549 (1990).

44. Thiel, C. W., Böttger, T. & Cone, R. L. Rare-earth-doped materials for applications in quantum information storage and signal processing. *Journal of Luminescence* **131**, 353–361 (2011).

45. Bottger, T., Sun, Y., Thiel, C. & Cone, R. Spectroscopy and dynamics of er3+: Y2sio5 at 1.5 mu m. *PHYSICAL REVIEW B* **74** (2006).

46. Gupta, S. *et al.* Dual epitaxial telecom spin-photon interfaces with long-lived coherence. *Nature Communications* **16**, 9814 (2025).

47. Xie, T. *et al.* Characterization of Er3+:YVO4 for microwave to optical transduction. *Physical Review B* **104**, 054111 (2021).

48. Zhu, D. *et al.* Integrated photonics on thin-film lithium niobate. *Advances in Optics and Photonics* **13**, 242–352 (2021).

49. Wang, S. *et al.* Incorporation of erbium ions into thin-film lithium niobate integrated photonics. *Applied Physics Letters* **116**, 151103 (2020).

50. Dibos, A. M. *et al.* Purcell enhancement of erbium ions in tio2 on silicon nanocavities. *Nano Letters* **22**, 6530–6536 (2022).

51. Zhang, J. *et al.* Optical and spin coherence of Er spin qubits in epitaxial cerium dioxide on silicon. *npj Quantum Information* **10**, 119 (2024).

52. Yin, C. *et al.* Optical addressing of an individual erbium ion in silicon. *Nature* **497**, 91–94 (2013).

53. Weiss, L., Gritsch, A., Merkel, B. & Reiserer, A. Erbium dopants in nanophotonic silicon waveguides. *Optica* **8**, 40–41 (2021).

54. Gritsch, A., Weiss, L., Früh, J., Rinner, S. & Reiserer, A. Narrow optical transitions in erbium-implanted silicon waveguides. *Physical Review X* **12**, 041009 (2022).

55. Prezzi, D. *et al.* Optical and electrical properties of vanadium and erbium in 4H-SiC. *Physical Review B* **69**, 193202 (2004).

56. Parker, R. A. *et al.* Infrared erbium photoluminescence enhancement in silicon carbide nanopillars. *Journal of Applied Physics* **130**, 145101 (2021).

57. Liu, D.-C. *et al.* On-demand storage of photonic qubits at telecom wavelengths. *Physical Review Letters* **129**, 210501 (2022).

58. Cornacchia, F., Toncelli, A. & Tonelli, M. Growth and spectroscopic characterization of Er3+:CaWO4. *Journal of Applied Physics* **101**, 123113 (2007).

59. Becker, F. *et al.* Spectroscopic investigations of multiple environments in Er:CaWO4 through charge imbalance. *Physical Review Materials* **9**, 076203 (2025).

60. Fleuster, M., Buchal, C., Snoeks, E. & Polman, A. Optical and structural properties of MeV erbium-implanted LiNbO3. *Journal of Applied Physics* **75**, 173–180 (1994).

61. Yang, L., Wang, S. & Tang, H. X. Toward radiative-limited coherence of erbium dopants in a nanophotonic resonator. *Applied Physics Letters* **123**, 124001 (2023).

62. Yan, L., Englert, A. H., Masliyah, J. H. & Xu, Z. Determination of anisotropic surface characteristics of different phyllosilicates by direct force measurements. *Langmuir* **27**, 12996–13007 (2011).

63. Zhang, M. *et al.* Dehydroxylation, proton migration, and structural changes in heated talc: An infrared spectroscopic study. *American Mineralogist* **91**, 816–825 (2006).

64. Freysoldt, C. *et al.* First-principles calculations for point defects in solids. *Reviews of modern physics* **86**, 253–305 (2014).

65. Freysoldt, C. & Neugebauer, J. First-principles calculations for charged defects at surfaces, interfaces, and two-dimensional materials in the presence of electric fields. *Physical Review B* **97**, 205425 (2018).

66. Weston, L., Wickramaratne, D., Mackoit, M., Alkauskas, A. & Van de Walle, C. Native point defects and impurities in hexagonal boron nitride. *Physical Review B* **97**, 214104 (2018).

67. Roemelt, M., Maganas, D., DeBeer, S. & Neese, F. A combined DFT and restricted open-shell configuration interaction method including spin-orbit coupling: Application to transition metal L-edge X-ray absorption spectroscopy. *The Journal of Chemical Physics* **138**, 204101 (2013). URL https://doi.org/10.1063/1.

4804607. https://pubs.aip.org/aip/jcp/article-pdf/doi/10.1063/1.4804607/13280319/204101_1_online.pdf.

68. Olsen, J. The casscf method: A perspective and commentary. *International Journal of Quantum Chemistry* **111**, 3267–3272 (2011).

69. Dodson, C. M. & Zia, R. Magnetic dipole and electric quadrupole transitions in the trivalent lanthanide series: Calculated emission rates and oscillator strengths. *Physical Review B* **86** (2012). URL http://dx.doi.org/10.1103/PhysRevB.86.125102.

70. Aharonovich, I., Englund, D. & Toth, M. Solid-state single-photon emitters. *Nature Photonics* **10**, 631–641 (2016).

71. Kim, S. *et al.* Photonic crystal cavities from hexagonal boron nitride. *Nature Communications* **9**, 2623 (2018).

72. Fröch, J. E. *et al.* Coupling hexagonal boron nitride quantum emitters to photonic crystal cavities. *ACS Nano* **14**, 7085–7091 (2020).

73. Parto, K. *et al.* Cavity-enhanced 2d material quantum emitters deterministically integrated with silicon nitride microresonators. *Nano Letters* **22**, 9748–9756 (2022).

74. Dibos, A. M., Raha, M., Phenicie, C. M. & Thompson, J. D. Atomic source of single photons in the telecom band. *Physical Review Letters* **120**, 243601 (2018).

75. Merkel, B., Ulanowski, A. & Reiserer, A. Coherent and purcell-enhanced emission from erbium dopants in a cryogenic high-q resonator. *Physical Review X* **10**, 041025 (2020).

76. Yang, L., Wang, S., Shen, M., Xie, J. & Tang, H. X. Controlling single rare earth ion emission in an electro-optical nanocavity. *Nature Communications* **14**, 1718 (2023).

77. Kresse, G. & Hafner, J. Ab initio molecular-dynamics simulation of the liquid-metal–amorphous-semiconductor transition in germanium. *Phys. Rev. B* **49**, 14251–14269 (1994). URL http://link.aps.org/doi/10.1103/PhysRevB.49.14251.

78. Kresse, G. & Furthmüller, J. Efficient iterative schemes for *ab initio* total-energy calculations using a plane-wave basis set. *Phys. Rev. B* **54**, 11169–11186 (1996). URL http://link.aps.org/doi/10.1103/PhysRevB.54.11169.

79. Furness, J. W., Kaplan, A. D., Ning, J., Perdew, J. P. & Sun, J. Accurate and numerically efficient r2scan meta-generalized gradient approximation. *Journal of Physical Chemistry Letters* **11**, 8208–8215 (2020).

80. Heyd, J., Scuseria, G. E. & Ernzerhof, M. Hybrid functionals based on a screened coulomb potential. *Journal of Chemical Physics* **118**, 8207–8215 (2003).

81. Krukau, A. V., Vydrov, O. A., Izmaylov, A. F. & Scuseria, G. E. Influence of the exchange screening parameter on the performance of screened hybrid functionals. *Journal of Chemical Physics* **125**, 224106 (2006).

82. Heyd, J., Scuseria, G. E. & Ernzerhof, M. Erratum: "hybrid functionals based on a screened coulomb potential" [Journal of Chemical Physics 118, 8207 (2003)]. *Journal of Chemical Physics* **124**, 219906 (2006).

83. Grimme, S., Antony, J., Ehrlich, S. & Krieg, H. A consistent and accurate ab initio parametrization of density functional dispersion correction (DFT-D) for the 94 elements H-Pu. *The Journal of Chemical Physics* **132**, 154104 (2010). URL https://doi.org/10.1063/1.3382344.

84. Blöchl, P. E. Projector augmented-wave method. *Phys. Rev. B* **50**, 17953–17979 (1994). URL http://link.aps.org/doi/10.1103/PhysRevB.50.17953.

85. Tunega, D. & Turi Nagy, L. Calculation of electron structure of talc by semiempirical methods of quantum chemistry. *Ceramics-Silikaty* **37**, 145–147 (1993). URL https://www.irsm.cas.cz/materialy/cs_content/1993/Tunega_CS_1993_0000.pdf.

86. Neese, F. The ORCA program system. *Wiley Interdisciplinary Reviews: Computational Molecular Science* **2**, 73–78 (2012).

87. Neese, F., Wennmohs, F., Becker, U. & Riplinger, C. The ORCA quantum chemistry program package. *The Journal of Chemical Physics* **152**, 224108 (2020).

88. Neese, F. Software update: The ORCA program system–version 6.0. *Wiley Interdisciplinary Reviews: Computational Molecular Science* **15**, e70019 (2025).

89. Roos, B. O., Taylor, P. R. & Siegbahn, P. E. M. A complete active space SCF method (CASSCF) using a density matrix formulated super-CI approach. *Chemical Physics* **48**, 157–173 (1980).

90. Sayfutyarova, E. R., Sun, Q., Chan, G. K.-L. & Knizia, G. Automated construction of molecular active spaces from atomic valence orbitals. *Journal of Chemical Theory and Computation* **13**, 4063–4078 (2017).

91. Ganyushin, D. & Neese, F. First-principles calculations of zero-field splitting parameters. *The Journal of Chemical Physics* **125**, 024103 (2006).

92. Ganyushin, D. & Neese, F. A fully variational spin–orbit coupled complete active space self-consistent field approach: Application to electron paramagnetic resonance g-tensors. *The Journal of Chemical Physics* **138**, 104113 (2013).

93. Lang, L., Chilkuri, V. G. & Neese, F. Treating spin–orbit coupling and spin–spin coupling in the framework of the iterative configuration expansion selected CI. *Journal of Chemical Theory and Computation* **21**, 6482–6504 (2025).

94. Neese, F. & Solomon, E. I. Calculation of zero-field splittings, g-values, and the relativistic nephelauxetic effect in transition metal complexes. application to high-spin ferric complexes. *Inorganic Chemistry* **37**, 6568–6582 (1998).

95. Hess, B. A., Marian, C. M., Wahlgren, U. & Gropen, O. A mean-field spin–orbit method applicable to correlated wavefunctions. *Chemical Physics Letters* **251**, 365–371 (1996).

96. Neese, F. Efficient and accurate approximations to the molecular spin–orbit coupling operator and their use in molecular g-tensor calculations. *The Journal of Chemical Physics* **122**, 034107 (2005).

97. Weigend, F. & Ahlrichs, R. Balanced basis sets of split valence, triple zeta valence and quadruple zeta valence quality for H to Rn: Design and assessment of accuracy. *Physical Chemistry Chemical Physics* **7**, 3297–3305 (2005).

98. Cao, X. & Dolg, M. Valence basis sets for relativistic energy-consistent small-core lanthanide pseudopotentials. *The Journal of Chemical Physics* **115**, 7348–7355 (2001).

99. Cao, X. & Dolg, M. Segmented contraction scheme for small-core lanthanide pseudopotential basis sets. *Journal of Molecular Structure: THEOCHEM* **581**, 139–147 (2002).

100. Weigend, F. Accurate coulomb-fitting basis sets for H to Rn. *Physical Chemistry Chemical Physics* **8**, 1057–1065 (2006).

101. Hellweg, A., Hättig, C., Höfener, S. & Klopper, W. Optimized accurate auxiliary basis sets for RI-MP2 and RI-CC2 calculations for the atoms Rb to Rn. *Theoretical Chemistry Accounts* **117**, 587–597 (2007).

102. Chmela, J. & Harding, M. E. Optimized auxiliary basis sets for density fitted post-Hartree–Fock calculations of lanthanide containing molecules. *Molecular Physics* **116**, 1523–1538 (2018).

Supplementary Files

This is a list of supplementary files associated with this preprint. Click to download.

- SItalcEr.pdf